ACS OMEGA

http://pubs.acs.org/journal/acsodf

Article

Enhanced Oxygen Evolution Reaction Activity in Hematite Photoanodes: Effect of Sb-Li Co-Doping

Paolo Rudatis, Jakob Hrubesch, Stefan Kremshuber, Dogukan H. Apaydin,* and Dominik Eder

Cite This: *ACS Omega* 2023, 8, 2027−2033

Read Online

ACCESS | Metrics & More | Article Recommendations | Supporting Information

ABSTRACT: Co-doping represents a valid approach to maximize the performance of photocatalytic and photoelectrocatalytic semiconductors. Albeit theoretical predictions in hematite suggesting a bulk n-type doping and a surface p-type doping would deliver best results, hematite co-doping with coupled cations possessing low and high oxidation states has shown promising results. Herein, we report, for the first time, Sb and Li co-doping of hematite photoanodes. Particularly, this is also a seminal work for the introduction of the highly reactive Sb^{5+} directly into the hematite thin films. Upon co-doping, we have a synergistic effect on the current densities with a 67-fold improvement over the standard. Via a combined investigation with profuse photoelectrochemical measurements, X-ray diffraction, X-ray photoelectron spectroscopy, and Raman analyses, we confirm the two doping roles of Sb^{5+} and Li^{+} as the substitutional and interstitial dopant, respectively. The improvements are attributed to a higher charge carrier concentration along with a lower charge transfer resistance at the surface.

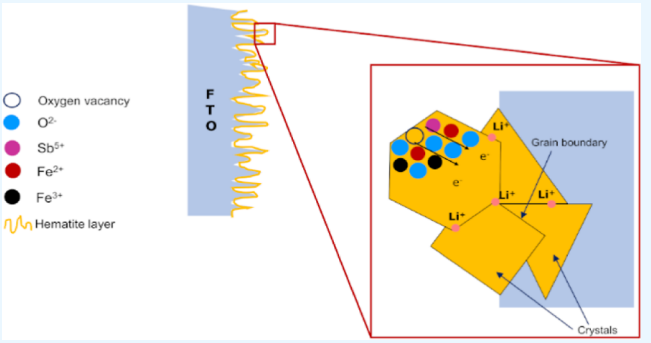

1. INTRODUCTION

Oxygen, the source of life on earth as well as the main component of diverse minerals, is produced via solar water splitting. Hydrogen, which is obtained through reduction half-reaction of water splitting, is considered as one of the most important candidates for a low-carbon economy.[1,2] There is ample research directed on the production of hydrogen using solar light.[3−6] Due to its sluggish kinetics, the oxidative part of the water splitting reaction, that is, oxygen evolution reaction (OER), requires catalysts capable of absorbing light and delivering fast charge transfer. Co-doping is one of the successful approaches in metal oxide photocatalysis and photoelectrocatalysis to further improve and understand the material properties.[7−11] Among several metal oxide catalysts, Hematite stands out as a promising candidate to be used in photoelectrochemical cells thanks to its band gap allowing to absorb most of the visible light, its stability, non-toxicity, and earth-abundant atoms.[12,13] Despite these positive aspects, hematite suffers from poor conductivity and low charge carrier diffusion length (2−4 nm for holes).[14,15] Short lifetimes of photo-generated carriers (10^{-12} s) and the inadequate band position add to the problem. Many transition metals have been introduced into hematite crystal lattice as extrinsic dopants for electron (Sn, Si, Nb, Sb, Zr, Ta, Rh, Ge, Ru, and Pt) and hole (Mg, Cu, Mn, Ru, and Ni) donors.[12,13,16−26] Hematite can also be doped intrinsically via oxygen vacancies.[27−29] Moreover, co-doping may be observed in cases where FTO is used as a substrate. The use of FTO leads to the diffusion of Sn^{4+} due to annealing at high temperatures.[16,30−32]

Tetravalent dopants are envisioned to introduce charge neutrality by donating $2e^{-}$ to neighbouring Fe^{3+} atoms in hematite. However, in reality, it is observed that Sn^{4+} induces only $0.3e^{-}$ on one Fe atom.[20,23,24] On the other hand, theoretical calculations have demonstrated that a pentavalent atom, such as a Sb^{5+} cation, can induce an overall charge distribution in four surrounding Fe atoms equal to a total of $2e^{-}$. The doping effect of pentavalent atoms like Sb^{5+} has not been explored experimentally. Furthermore, theory suggests that double donor doping can create two Fe^{2+} cations, positively affecting the hopping characteristics of charge carriers in hematite.[33,34] One possible candidate for double-doping are Li^{+}-ions. Li^{+}-doping of iron oxide has been investigated[35] and tested successfully for Li-ion batteries.[36,37] To date, there is only one study[38] showing Li^{+}-doped hematite with respect to photoelectrocatalytic applications and none that combines both.

Received: August 16, 2022
Accepted: December 1, 2022
Published: January 4, 2023

By considering the charge transfer band and upper Hubbard band, the most promising approach appears to be bulk n-type doping and a surface p-type doping.[39] However, not only the photo-generated charge carriers do not live long in hematite, but there are also further issues, that is, a poor photogeneration yield and a weak charge separation yield.[26,40] The latter can be influenced by a strategic co-doping with n−p-type doping centers, which in turn could enhance the charge separation yield.[26]

In this work, we explored for the first time the role of Sb^{5+} and Li^{+} as co-dopants in the hematite photoanode to create eventual fast-charge-separating p−n type centers. We successfully achieved *in situ* hematite doping using chloride-based precursor solutions. The effects of co-doping on hematite photoelectrodes were characterized by X-ray photoelectron spectroscopy (XPS), grazing incidence X-ray diffraction (XRD), and Raman spectroscopy. Photoelectrochemical tests confirm that both Sb^{5+} and Li^{+} cations can enhance the output photocurrent, highlighting a synergistic effect by this co-doping strategy.

2. RESULTS AND DISCUSSION

2.1. Structural Characteristics of Fe_2O_3 Photoanodes.

Figure 1 shows the UV−vis spectra of hematite (from here on, it will be denoted as Std.) and the singly doped and co-doped samples. At a first glance, the overall absorption performance of the samples appears similar: all show the typical peaks of hematite.[41−44] A closer look, however, reveals a small blue shift of the most intense peak composed of two individual absorption bands. The one at higher energy is expected at 375 nm and the one at lower can be identified at around 420 nm, where the curve flattening begins its descent to lower intensities. Both the peak at 420 nm as well as an additional peak at about 490 nm arise from spin-flip transitions, $2t_{2g}$, and $3e_g$. Here, magnetic coupling offers higher intensities of the peaks. Instead, due to spin-forbidden ligand field transitions, two peaks can be found. A distinctive peak is at around 535 nm, and a smaller one is expected at 600 nm; the latter appears as a shoulder.

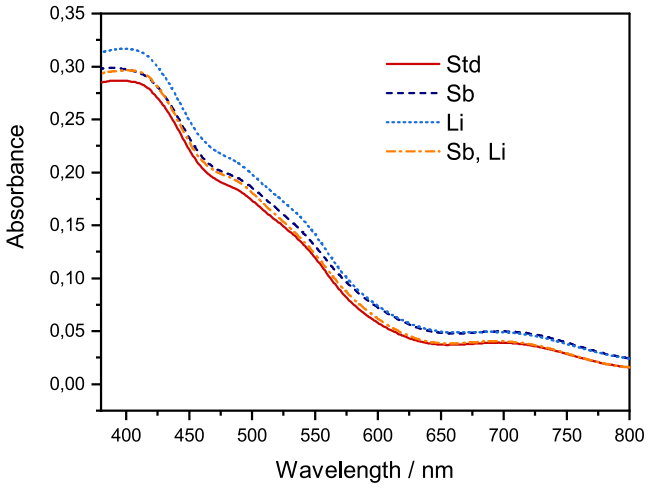

Figure 1. UV−vis absorption spectra of the hematite photoanodes.

Considering this, we notice that all the doped samples, mono- or co-doped, are capable of enhancing the light absorption to some extent. The increase is not large, though it is in line with small doping amounts (1 at. %) in nm-thick films. Certainly, an advantage is the diverse behavior and the presence of the additional monodoping photoanodes. In detail, on the one hand, the doping with Sb seems to allow for a general growth of absorption intensity compared with the undoped hematite sample. On the other hand, Li doping boosts the absorption intensity especially at wavelengths <550 nm, involving $2t_{2g}$, $3e_g$, and the spin-forbidden ligand field transition at higher energy. A similar Li-doping effect is observed in $BiVO_4$, both in transmittance mode[45] and in absorbance mode.[46] This is likely caused by the creation of shallow and deep acceptor levels.[47,48] Instead, Sb doping might enhance the absorption intensity because of band gap narrowing, as it happens in comparable semiconductors.[49,50] Nevertheless, as we do not observe any clear shift, the evenly augmented absorption intensity is likely attributable to other reasons, such as a more defective bulk with smaller crystals size and, hence, more grain boundaries.

Hematite belongs to the D^6_{3d} crystal space group, and thus, seven modes in total are expected, that is, two modes with A_{1g} symmetry and five modes with E_g symmetry. The former ones represent the movement of the Fe atoms on the defined unit cell *c*-axis, while the latter ones are visualized with the O atoms breathing modes in perpendicular to the *c*-axis. The micro-Raman spectra (Figure 2) display the A_{1g} bands at 217 and 490 cm^{-1} and the E_g bands at 238, 284, 400, and 603 cm^{-1}. Additional peaks at around 650 and 1301 cm^{-1} are the ungerade symmetry modes (E_u and $2E_u$), which usually should not be allowed. Owing to disorder, in the presence of magnetite, such modes can be permitted.[51−54] This is already true for the non-doped sample, which displays the E_u mode with a shoulder beside the E_g band at 603 cm^{-1}. Nonetheless, through the mode, we can recognize Sb-doped samples, as they exhibit a peak with identical shape, that is, this peak is sharp and overtakes in intensity the near band at lower wavenumbers. The Li-doped sample does not clearly display a variation from the standard. Such observation is in contrast with the Sb-doping effect, and it may suggest interstitial doping. The results from the Raman spectra confirm that the hematite is the main phase and that the films are made of nanocrystals.[54,55] Furthermore, with 650 cm^{-1} E_u mode, we substantiate the presence of both the two dopants we add, Sb^{5+} and Li^{+}.

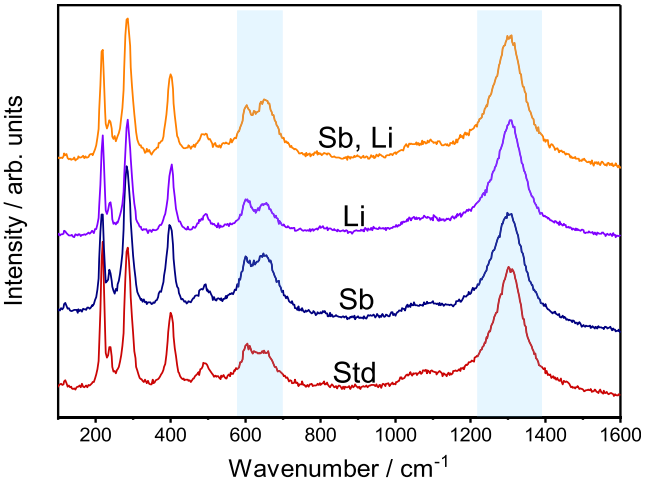

Figure 2. Micro-Raman spectra of standard, Sb monodoped, Li monodoped, and Sb/Li co-doped samples.

https://doi.org/10.1021/acsomega.2c05241
ACS Omega 2023, 8, 2027−2033

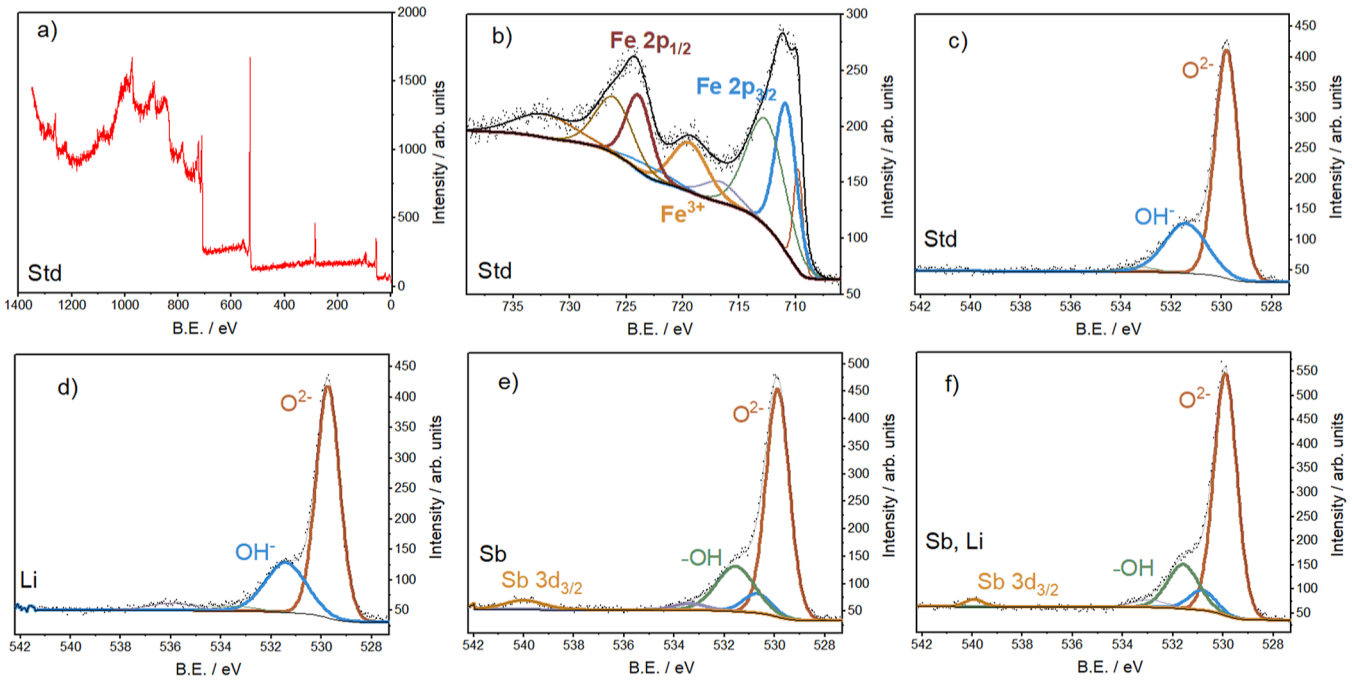

Figure 3. (a) XPS survey spectrum of the standard hematite sample. (b) Fe element XPS detail spectrum of the undoped sample. (c) O, Sb elements XPS detail spectrum of the standard sample. (d) O, Sb elements XPS detail spectrum of the Li monodoped sample. (e) O, Sb elements XPS detail spectrum of the Sb monodoped sample (f) O, Sb elements XPS detail spectrum of the Sb, Li co-doped sample.

The XPS survey spectrum shows the typical peaks of hematite films (Figure 3a). The short average penetration depth (<5 nm) of the X-ray photoelectrons limits elemental detection to the surface, and thus, it does not allow for identification of Sn and Fe in the bulk of the investigated samples. The peaks of Fe and O belong to the surface of the hematite thin layer. Furthermore, C occurs in relevant amount, about 29 at. % as adventitious carbon at the surface.

By scanning a binding energy (BE) range of 700−740 eV at lower intensity (Figure 3b), we intercept the signal associated with electrons occupying Fe 2p orbitals. This detailed spectrum displays the most intense peaks at about BE 711 and 724 eV, Fe $2p_{3/2}$ and Fe $2p_{1/2}$, respectively. Those peaks also have defined satellites at 8−9 eV higher than their BE. Components and satellite BEs are a good indication of Fe^{3+} cations, and thus it occurs in both samples. We could not identify further signals corresponding to Fe^{2+} species. The other sample spectra resemble the standard and we do not notice alterations after monodoping and co-doping (Figure S1). However, regarding the doping confirmation, more interesting results are offered by the O 1s/Sb 3d region (Figure 3c−e). The investigated range expands from BE 527 to 542 eV. Herein, we see two defined signals—one at lower BE and one at higher BE. The former is a mixture of O 1s components, while the latter is of Sb $3d_{5/2}$ arising from the spin−orbit component of Sb, that is, Sb $3d_{3/2}$. Upon deconvolution of the former one, we assign the most intense peak of the signal to O^{2-} anions at BE 529.90 eV. At higher BE of the same signal, a peak appears among BE 531.4−531.6 eV, which is assigned to Fe−O bonding, for example, hydroxy groups (−OH).[29,56,57] At around 533−533.5 eV, we find another minor peak that may arise from hydrocarbons, likely as surface contaminations.[58,59] The Sb $3d_{3/2}$ component lies around BE 539.96 ± 0.04 eV and does not carry the complication of a fitting. This further substantiates that the precursor and annealing lead to Sb^{5+}-doping of hematite.[20,60] Unfortunately, Li^{+}-doping cannot be identified directly, since two more intense Fe 3p components overlap with it. The Li 1s peak is expected at BE 55−56 eV, while the Fe 3p components range from BE 54 to 58 eV.[35] XRD measurements can shine light onto the presence of dopant ions in this case.

The diffractograms prevalently show the underneath FTO substrate (# symbols in Figure 4), albeit the adopted lowest 2°

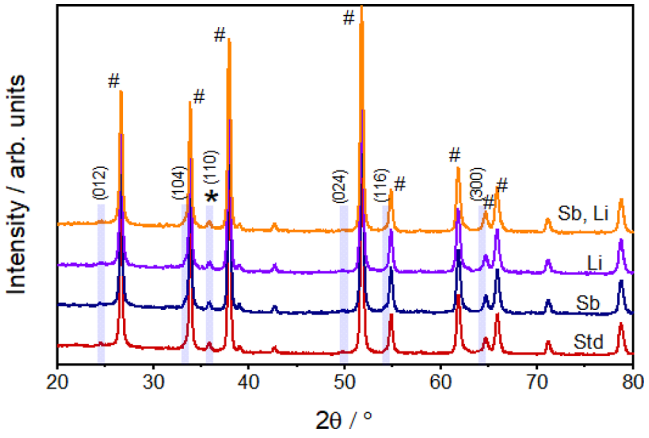

Figure 4. XRD patterns of the standard sample, Sb and Li monodoped samples, and Sb and Li co-doped sample.

grazing incidence diffraction angle. In Figure 4, we do not observe significant differences of the substrate after doping and co-doping. The most intense peak of crystalline hematite (110) appears, and it is distinctive. The same cannot be observed for the less pronounced peaks of hematite [(012) (104) (024) (116) (300)].

With a closer look at the (110) diffraction peaks of the batch samples, we detect relevant variations (Figure S2). Non-doped

https://doi.org/10.1021/acsomega.2c05241
ACS Omega 2023, 8, 2027−2033

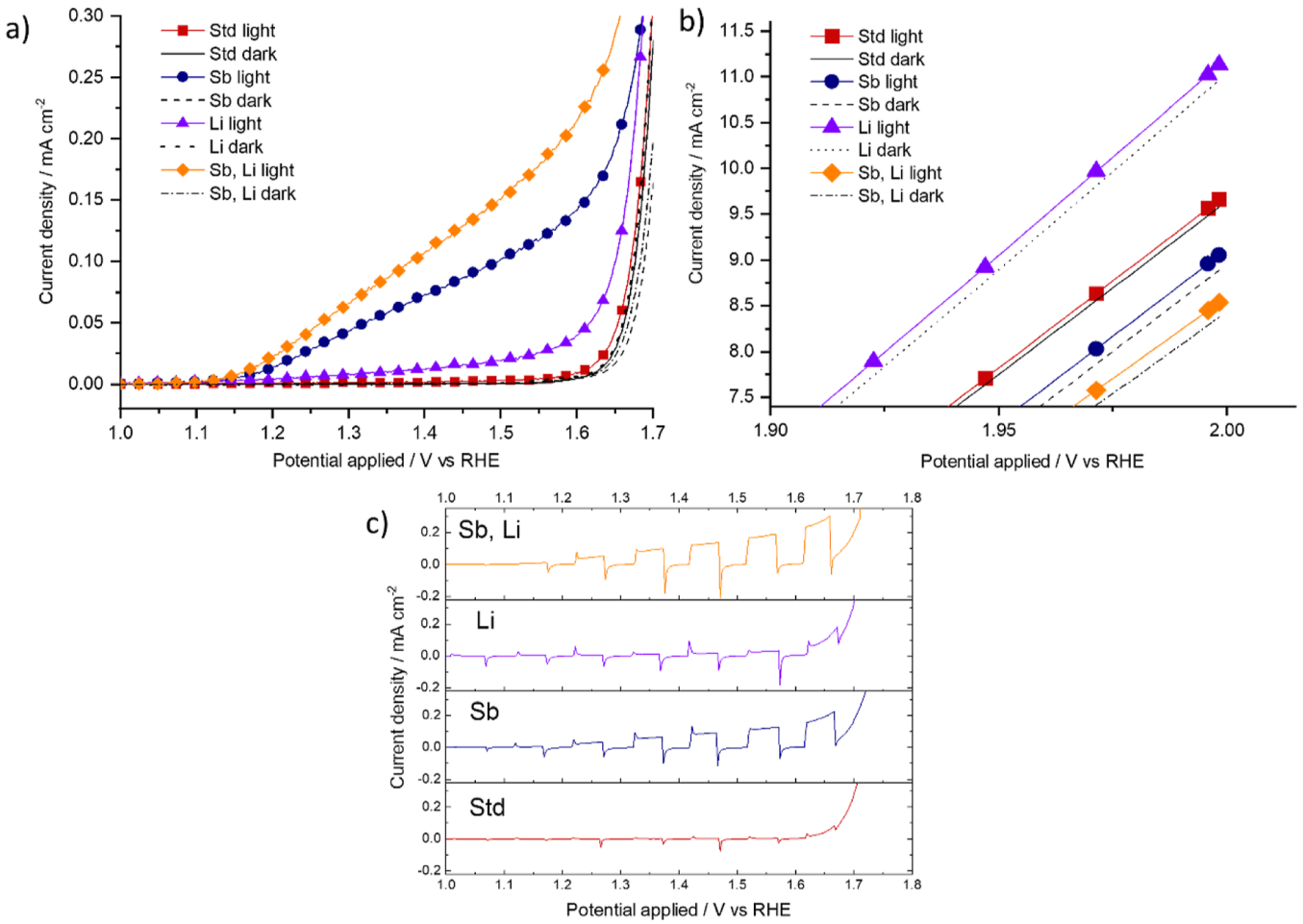

Figure 5. (a) $J-V$ curves light and dark recorded in 0.1 M NaOH with the calomel electrode and Pt cathode. The potentials are reported *vs* RHE. Light curves were carried out under a simulated solar light illumination of 100 mW cm^{-2}. (b) $J-V$ behavior in the Faradaic regime. (c) $J-V$ curves under chopped illumination.

and Sb monodoped sample (110) peaks reach their maximum at 2θ about 37.97°. On the contrary, both XRD patterns of the Li-doped samples, monodoped and co-doped, exhibit a gentle shift toward lower 2θ values at 37.95°. Albeit the observed gap is small, it occurs only after the introduction of Li cations. This observation suggests that Li cations added with 1% can access the hematite lattice exclusively as interstitial dopants.[61,62] The aforementioned results support the substitutional introduction of Sb into the hematite lattice.[20,60] In addition, these results are in agreement with the XPS findings, that is, oxygen vacancies do not affect singularly the samples and hence counterfeiting the photo- and electrochemical performances.[63]

2.2. Photoelectrochemical Performance of Fe_2O_3 Photoanodes. The $J-V$ curves for the hematite reference show a steep increase in current at around 1.6 V, similar to those curves reported in literature.[14,16,64,65] Figure 5a shows that doping with Li^+ and Sb^{5+} increases the photocurrent at lower potentials significantly. At 1.4 V *versus* RHE, the introduction of Li^+ cations offers a moderate increase in photocurrent by about eight-fold compared to the reference. This effect is even more pronounced with Sb^{5+}-doping, which enhances the photocurrent by 45 times. Note that the co-doping of the two cations enhances the photoelectrochemical performance by 67-fold, which indicates a synergistic effect of the two ions. At 1.6 V *versus* RHE, the relative enhancements are slightly lower, that is, 4-, 15-, and 23-fold for the Li^+, Sn^{5+}, and co-doped samples, respectively. Curiously, the on-set potentials of the $J-V$ curves under illumination are not significantly affected by any of the doping strategies. At around 2 V *versus* RHE, the regime of the current density is almost completely Faradaic (Figure 5b). Here, we witness that the trend observed previously in the photoelectrochemical characterization does change. This gives the opportunity to observe the material behavior without the constraints of charge separation. Except Li^+ monodoping, the observation is that the higher the photoactivity, the lower the current density at high applied voltages. At 2 V *versus* RHE, the current densities of dark $J-V$ curves of non-doped, Sb-doped, and Sb, Li-co doped samples reach 9.6, 8.9, and 8.4 mA cm^{-2}, respectively. Exceptionally, Li^+-doping shows a remarkable current density that stops marginally below 11 mA cm^{-2} (black line). To date, this current density is the highest within the simple, solution-based methods. Figure 5c presents the chopped light $J-V$ curves, which display the typical current transients. The positive current transients, that is, increasing spikes, testify that not all the holes that reach the interface contribute to the OER, while the negative current transients mean that there is recombination between electrons and photo-oxidized surface species.[66,67] In order to have a better and faster understanding of the numerical result of chopped light $J-V$ curves, we find it convenient to calculate the ratio of the spike and steady currents over the average photocurrent in the range of 1.3−1.4

https://doi.org/10.1021/acsomega.2c05241
ACS Omega 2023, 8, 2027−2033

V *versus* RHE, which yield the percent efficiency for holes being used in water oxidation.[38,66,68] The non-doped sample displays a charge extraction efficiency of 20%. Li-doping can double the efficiency to about 43%. Meanwhile, Sb-doping has yielded almost 63% efficiency. Finally, upon co-doping, the charge conversion efficiency has reached 91%. Furthermore, we expect Sb-doping to increase the carrier concentration and decrease the interfacial charge transfer resistance, which is evident both by XPS and XRD results as well as by the increase in the efficiency for charge extraction.[20] By contrast, as seen in XRD, we expect Li^+ to enter the hematite film only interstitially and thus it mainly leads to an expanded majority carrier concentration.[45] Those theories are also consistent with the high current density of the Li-doped sample (Figure 5b) and the increased charge extraction efficiency (Figure 5c). As we have substantiated that Li^+ is an interstitial dopant for our hematite photoanodes, leaching experiments were carried out to exclude that Li^+ could leach out of the thin films into the electrolyte. After adding LiCl to a final 0.01 M concentration into the typical NaOH 0.1 M electrolyte, the samples shown in Figure 5 were measured one more time (Figure S3). As a result, the trend is maintained, while the photoactivity is generally lower (Figure S3a). The gauged photocurrent at 1.4 V *versus* RHE goes from 0.11 to 0.07 mA cm^{-2}, which translates into a 1.6-fold (or 36%) relative reduction. Also, in the Faradaic regime, a general current decrease with the Li buffering is still observed (Figure S3b). By comparing the chopped light $J-V$ curves (Figure S3c,d), namely, before and after the Li addition, a shrinkage of the charge extraction efficiency is observed. In detail, the efficiency lessens from a value of 91−55%. This means that the photogenerated surface holes seem to recombine more, rather than lead to OER. Although there might be an aging effect because of the prolonged photoanode storage, it can be deducted that Li cations should not permeate in and out the annealed hematite thin film. Diversely, the photocurrents would be affected singularly, hence considerably modifying the prior trend.

3. CONCLUSIONS

In short, the Sb and Li co-doping of hematite thin films is beneficial and leads to a 67-fold improvement on the photoelectrochemical performance at 1.4 V *versus* RHE. Interestingly, the increment on the photocurrent by Sb and Li-doping appears to be a synergistic effect. According to the photoelectrochemical analysis, both dopants augment the carrier concentration, and particularly, Sb diminishes the charge transfer resistance at the interface. This effect is particularly clear when comparing Sb monodoped and Sb, Li co-doped samples in chopped light LSV. The utilization of a direct Sb^{5+} cation source has the advantage to assure a unique Sb^{5+}-doping in the hematite lattice even at lower annealing temperatures.

Further characterization is needed to shine light on the kinetics of photo-generated charge carriers and to verify whether Sb, Li co-doping also enables an increased charge separation yield and prolongs carriers' lifetimes. Therefore, this paper lays the foundation for further utilization of co-doping in other metal oxide semiconductors for photocatalysis and photoelectrocatalysis.

4. METHODS

All the chemicals were used as they received unless mentioned otherwise.

4.1. Preparation of Photoanodes. In a typical solution, $FeCl_3{\cdot}6H_2O$ (Fluka, 99%) (0.54 g) was dissolved in 20 mL of DI water. Under gentle stirring, polyethylenglycol bisphenol A epichlorhydrin (Sigma-Aldrich, 15000−20000 Da) (0.54 g) was also added and dissolved. An FTO slide was masked with a Kapton tape to keep the first 0.5 cm of the electrode free for ohmic contact. 2 mL of the solution was deposited onto the FTO slide and it was spin-coated at 1000 rpm. This procedure was repeated four times to achieve sufficient thickness for light absorption (Figure S4). After each deposition, the Kapton tape was removed, and the electrode was annealed at 550 °C to form hematite. The electrode was then cut into photoanodes with a photoactive area of 1 × 1 cm.

4.2. Doping of Hematite. In order to dope hematite *in situ*, the precursors for co-doping were added directly to the spin-coating solutions. However, to enhance the reproducibility and minimize errors, the amount of precursors are taken from mother solutions. LiCl (Sigma-Aldrich, ≥99%) (0.0424 g, 0.001 mol) was dissolved in 10 mL of DI water to obtain a 0.1 M solution. To get the same solution concentration, $SbCl_5$ (Sigma-Aldrich, 99%) (0.299 g, 0.001 mol) was dissolved in 10 mL of concentrated HCl (36%). Therefore, to add a nominal 1 at. % of dopants over mol of formed Fe_2O_3, 100 μL needed to be transferred to the respective spin-coating solution. Four solutions were prepared including standard samples, two monodoped samples (Sb^{5+} and Li^+) and the co-doped sample. HCl greatly inhibits the hydrolyzation and stabilizes the solution. No signs of hydrolysis were observed in the Sb^{5+} mother solution after about 2 years of storage. As water and concentrated HCl were added to dope the spin-coating solutions, all the solutions were compensated with the missing solvents.

■ ASSOCIATED CONTENT

Supporting Information

The Supporting Information is available free of charge at https://pubs.acs.org/doi/10.1021/acsomega.2c05241.

XPS, XRD data, as well as voltammograms and SEM images (PDF)

■ AUTHOR INFORMATION

Corresponding Author

Dogukan H. Apaydin − *Institute of Materials Chemistry, TU Wien, Wien 1060, Austria;* orcid.org/0000-0002-1075-8857; Email: dogukan.apaydin@tuwien.ac.at

Authors

Paolo Rudatis − *Institute of Materials Chemistry, TU Wien, Wien 1060, Austria*

Jakob Hrubesch − *Institute of Materials Chemistry, TU Wien, Wien 1060, Austria*

Stefan Kremshuber − *Institute of Materials Chemistry, TU Wien, Wien 1060, Austria;* orcid.org/0000-0003-2444-1727

Dominik Eder − *Institute of Materials Chemistry, TU Wien, Wien 1060, Austria;* orcid.org/0000-0002-5395-564X

Complete contact information is available at: https://pubs.acs.org/10.1021/acsomega.2c05241

https://doi.org/10.1021/acsomega.2c05241
ACS Omega 2023, 8, 2027−2033

Author Contributions

The manuscript was written through contributions of all authors. All authors have given approval to the final version of the manuscript.

Funding

The authors gratefully acknowledge the funding within the framework of "Solarreaktor" project supported by the Austrian Research Promotion Agency (FFG).

Notes

The authors declare no competing financial interest.

■ ACKNOWLEDGMENTS

The authors gratefully acknowledge Bernhard Fickl for the Raman measurements. The authors acknowledge TU Wien Bibliothek for financial support through its Open Access Funding Programme.

■ REFERENCES

(1) IEA. *The Future of Hydrogen*; Seizing Today's Opportunities: Japan, 2019.
(2) Gielen, D.; Taibi, E.; Miranda, R. *Hydrogen*; A Renewable Energy Perspective, 2019.
(3) Boumeriame, H.; Da Silva, E. S.; Cherevan, A. S.; Chafik, T.; Faria, J. L.; Eder, D. Layered Double Hydroxide (LDH)-Based Materials: A Mini-Review on Strategies to Improve the Performance for Photocatalytic Water Splitting. *J. Energy Chem.* **2022**, *64*, 406−431.
(4) Zhao, W.; Chen, Z.; Yang, X.; Qian, X.; Liu, C.; Zhou, D.; Sun, T.; Zhang, M.; Wei, G.; Dissanayake, P. D.; Ok, Y. S. Recent Advances in Photocatalytic Hydrogen Evolution with High-Performance Catalysts without Precious Metals. *Renew. Sustain. Energy Rev.* **2020**, *132*, 110040.
(5) Zhu, J.; Hu, L.; Zhao, P.; Lee, L. Y. S.; Wong, K.-Y. Recent Advances in Electrocatalytic Hydrogen Evolution Using Nanoparticles. *Chem. Rev.* **2020**, *120*, 851−918.
(6) Dubouis, N.; Grimaud, A. The Hydrogen Evolution Reaction: From Material to Interfacial Descriptors. *Chem. Sci.* **2019**, *10*, 9165−9181.
(7) Sun, Z.; Fang, G.; Li, J.; Mo, J.; He, X.; Wang, X.; Yu, Z. Preparation of (Ti, Zr) Co-Doped Hematite Photoanode for Enhanced Photoelectrochemical Water Splitting. *Chem. Phys. Lett.* **2020**, *754*, 137736.
(8) Wang, J.; Du, C.; Peng, Q.; Yang, J.; Wen, Y.; Shan, B.; Chen, R. Enhanced Photoelectrochemical Water Splitting Performance of Hematite Nanorods by Co and Sn Co-Doping. *Int. J. Hydrogen Energy* **2017**, *42*, 29140−29149.
(9) Luo, H.; Takata, T.; Lee, Y.; Zhao, J.; Domen, K.; Yan. Photocatalytic Activity Enhancing for Titanium Dioxide by Co-Doping with Bromine and Chlorine. *Chem. Mater.* **2004**, *16*, 846−849.
(10) Prasad, U.; Young, L.; McGott, C.; Garfunkel, L.; Kannan, H. Enhancing interfacial charge transfer in a WO3/BiVO4 photoanode heterojunction through gallium and tungsten co-doping and a sulfur modified Bi2O3 interfacial layer. *J. Mater. Chem. A* **2021**, *9*, 16137−16149.
(11) Venkata Reddy, C.; Reddy, I. N.; Akkinepally, B.; Reddy, K. R.; Shim, J. Synthesis and photoelectrochemical water oxidation of (Y, Cu) codoped α-Fe2O3 nanostructure photoanode. *J. Alloys Compd.* **2020**, *814*, 152349.
(12) Yoon, K.-Y.; Park, J.; Jung, M.; Ji, S.-G.; Lee, H.; Seo, J. H.; Kwak, M.-J.; Il Seok, S.; Lee, J. H.; Jang, J.-H. NiFeOx Decorated Ge-Hematite/Perovskite for an Efficient Water Splitting System. *Nat. Commun.* **2021**, *12*, 4309.
(13) Zhang, H.; Li, D.; Byun, W. J.; Wang, X.; Shin, T. J.; Jeong, H. Y.; Han, H.; Li, C.; Lee, J. S. Gradient Tantalum-Doped Hematite Homojunction Photoanode Improves Both Photocurrents and Turn-on Voltage for Solar Water Splitting. *Nat. Commun.* **2020**, *11*, 4622.
(14) Kennedy, J. H.; Frese, K. W. Photooxidation of Water at α - Fe2 O 3 Electrodes. *J. Electrochem. Soc.* **1978**, *125*, 709−714.
(15) Sivula, K.; Formal, F. L.; Grätzel, M. WO3−Fe2O3 Photoanodes for Water Splitting: A Host Scaffold, Guest Absorber Approach. *Chem. Mater.* **2009**, *21*, 2862−2867.
(16) Ling, Y.; Wang, G.; Wheeler, D. A.; Zhang, J. Z.; Li, Y. Sn-Doped Hematite Nanostructures for Photoelectrochemical Water Splitting. *Nano Lett.* **2011**, *11*, 2119−2125.
(17) Orlandi, M.; Mazzi, A.; Arban, G.; Bazzanella, N.; Rudatis, P.; Caramori, S.; Patel, N.; Fernandes, R.; Bignozzi, C. A.; Miotello, A. On the Effect of Sn-Doping in Hematite Anodes for Oxygen Evolution. *Electrochim. Acta* **2016**, *214*, 345−353.
(18) Dias, P.; Lopes, T.; Andrade, L.; Mendes, A. Temperature Effect on Water Splitting Using a Si-Doped Hematite Photoanode. *J. Power Sources* **2014**, *272*, 567−580.
(19) Fu, Y.; Dong, C.-L.; Lee, W.-Y.; Chen, J.; Guo, P.; Zhao, L.; Shen, S. Nb-Doped Hematite Nanorods for Efficient Solar Water Splitting: Electronic Structure Evolution versus Morphology Alteration. *ChemNanoMat* **2016**, *2*, 704−711.
(20) Annamalai, A.; Sandström, R.; Gracia-Espino, E.; Boulanger, N.; Boily, J.-F.; Mühlbacher, I.; Shchukarev, A.; Wågberg, T. Influence of Sb5+ as a Double Donor on Hematite (Fe3+) Photoanodes for Surface-Enhanced Photoelectrochemical Water Oxidation. *ACS Appl. Mater. Interfaces* **2018**, *10*, 16467−16473.
(21) Jeong, I. K.; Mahadik, M. A.; Hwang, J. B.; Chae, W.-S.; Choi, S. H.; Jang, J. S. Lowering the onset potential of Zr-doped hematite nanocoral photoanodes by Al co-doping and surface modification with electrodeposited Co-Pi. *J. Colloid Interface Sci.* **2021**, *581*, 751−763.
(22) Kim, J. Y.; Magesh, G.; Youn, D. H.; Jang, J.-W.; Kubota, J.; Domen, K.; Lee, J. S. Single-Crystalline, Wormlike Hematite Photoanodes for Efficient Solar Water Splitting. *Sci. Rep.* **2013**, *3*, 1−8.
(23) Lin, Y.; Xu, Y.; Mayer, M. T.; Simpson, Z. I.; McMahon, G.; Zhou, S.; Wang, D. Growth of P-Type Hematite by Atomic Layer Deposition and Its Utilization for Improved Solar Water Splitting. *J. Am. Chem. Soc.* **2012**, *134*, 5508−5511.
(24) Liao, P.; Carter, E. A. Hole Transport in Pure and Doped Hematite. *J. Appl. Phys.* **2012**, *112*, 013701.
(25) Rauf, A.; Adil, M.; Mian, S. A.; Rahman, G.; Ahmed, E.; Mohy Ud Din, Z.; Qun, W. Tuning the Optoelectronic Properties of Hematite with Rhodium Doping for Photoelectrochemical Water Splitting Using Density Functional Theory Approach. *Sci. Rep.* **2021**, *11*, 41.
(26) Guo, X.; Wang, L.; Tan, Y. Hematite Nanorods Co-Doped with Ru Cations with Different Valence States as High Performance Photoanodes for Water Splitting. *Nano Energy* **2015**, *16*, 320−328.
(27) Yang, T.-Y.; Kang, H.-Y.; Sim, U.; Lee, Y.-J.; Lee, J.-H.; Koo, B.; Nam, K.; Joo, Y.-C. A New Hematite Photoanode Doping Strategy for Solar Water Splitting: Oxygen Vacancy Generation. *Phys. Chem. Chem. Phys.* **2013**, *15*, 2117−2124.
(28) Forster, M.; Potter, R. J.; Ling, Y.; Yang, Y.; Klug, D. R.; Li, Y.; Cowan, A. J. Oxygen deficient α-Fe2O3 photoelectrodes: a balance between enhanced electrical properties and trap-mediated losses. *Chem. Sci.* **2015**, *6*, 4009−4016.
(29) Wang, Z.; Mao, X.; Chen, P.; Xiao, M.; Monny, S. A.; Wang, S.; Konarova, M.; Du, A.; Wang, L. Understanding the Roles of Oxygen Vacancies in Hematite-Based Photoelectrochemical Processes. *Angew. Chem.* **2019**, *131*, 1042−1046.
(30) Sivula, K.; Zboril, R.; Le Formal, F.; Robert, R.; Weidenkaff, A.; Tucek, J.; Frydrych, J.; Grätzel, M. Photoelectrochemical Water Splitting with Mesoporous Hematite Prepared by a Solution-Based Colloidal Approach. *J. Am. Chem. Soc.* **2010**, *132*, 7436−7444.
(31) Zhou, Y.; Yan, M.; Hou, J.; Niu, Y.; Ni, D.; Shen, H.; Niu, P.; Ma, Y. Introduction of Oxygen Vacancies into Hematite in Local Reducing Atmosphere for Solar Water Oxidation. *Sol. Energy* **2019**, *179*, 99−105.
(32) Pyeon, M.; Ruoko, T.-P.; Leduc, J.; Gönüllü, Y.; Deo, M.; Tkachenko, N. V.; Mathur, S. Critical Role and Modification of

https://doi.org/10.1021/acsomega.2c05241
ACS Omega 2023, 8, 2027−2033

Surface States in Hematite Films for Enhancing Oxygen Evolution Activity. *J. Mater. Res.* **2018**, *33*, 455−466.
(33) Papaioannou, J. C.; Patermarakis, G. S.; Karayianni, H. S. Electron hopping mechanism in hematite (α-Fe2O3). *J. Phys. Chem. Solids* **2005**, *66*, 839−844.
(34) Ling, Y.; Wang, G.; Reddy, J.; Wang, C.; Zhang, J. Z.; Li, Y. The Influence of Oxygen Content on the Thermal Activation of Hematite Nanowires. *Angew. Chem.* **2012**, *124*, 4150−4155.
(35) Barik, R.; Pandey, B.; Anand, S.; Mohapatra, M. A Facile, Single-Step Synthesis of Flowery Shaped, Pure/Lithium-Doped 3D Iron Oxides. *J. Mater. Chem. A* **2014**, *2*, 12380−12389.
(36) Lu, J.; Peng, Q.; Wang, Z.; Nan, C.; Li, L.; Li, Y. Hematite Nanodiscs Exposing (001) Facets: Synthesis, Formation Mechanism and Application for Li-Ion Batteries. *J. Mater. Chem. A* **2013**, *1*, 5232−5237.
(37) Kim, H.-J.; Choi, K.-I.; Pan, A.; Kim, I.-D.; Kim, H.-R.; Kim, K.-M.; Na, C.; Cao, G.; Lee, J.-H. Template-Free Solvothermal Synthesis of Hollow Hematite Spheres and Their Applications in Gas Sensors and Li-Ion Batteries. *J. Mater. Chem.* **2011**, *21*, 6549−6555.
(38) Cai, J.; Xu, L.; Tang, X.; Kong, L.; Wang, J.; Wang, R.; Li, X.; Xie, Q.; Mao, K.; Pan, H. Role of lithium doping on α-Fe2O3 photoanode for enhanced photoelectrochemical water oxidation. *J. Alloys Compd.* **2022**, *915*, 165349.
(39) Zhang, J.; Eslava, S. Understanding Charge Transfer, Defects and Surface States at Hematite Photoanodes. *Sustain. Energy Fuels* **2019**, *3*, 1351−1364.
(40) Piekner, Y.; Ellis, S.; Tsyganok, A.; Rothschild, A.; Rothschild, A. Wasted Photons: Photogeneration Yield and Charge Carrier Collection Efficiency of Hematite Photoanodes for Photoelectrochemical Water Splitting. *Energy Environ. Sci.* **2021**, *14*, 4584−4598.
(41) Marusak, L. A.; Messier, R.; White, W. B. Optical absorption spectrum of hematite, αFe2O3 near IR to UV. *J. Phys. Chem. Solids* **1980**, *41*, 981−984.
(42) Itoh, K.; Bockris, J. O. Thin Film Photoelectrochemistry: Iron Oxide. *J. Electrochem. Soc.* **1984**, *131*, 1266.
(43) Bjoerksten, U.; Moser, J.; Graetzel, M. Photoelectrochemical Studies on Nanocrystalline Hematite Films. *Chem. Mater.* **1994**, *6*, 858−863.
(44) Beermann, N.; Vayssieres, L.; Lindquist, S.-E.; Hagfeldt, A. Photoelectrochemical Studies of Oriented Nanorod Thin Films of Hematite. *J. Electrochem. Soc.* **2000**, *147*, 2456−2461.
(45) Zhou, C.; Sanders-Bellis, Z.; Smart, T. J.; Zhang, W.; Zhang, L.; Ping, Y.; Liu, M. Interstitial Lithium Doping in BiVO4 Thin Film Photoanode for Enhanced Solar Water Splitting Activity. *Chem. Mater.* **2020**, *32*, 6401−6409.
(46) Prakash, J.; Prasad, U.; Shi, X.; Peng, X.; Azeredo, B.; Kannan, A. M. Photoelectrochemical Water Splitting Using Lithium Doped Bismuth Vanadate Photoanode with Near-Complete Bulk Charge Separation. *J. Power Sources* **2020**, *448*, 227418.
(47) Meyer, B. K.; Sann, J.; Zeuner, A. Lithium and Sodium Acceptors in ZnO. *Superlattices Microstruct.* **2005**, *38*, 344−348.
(48) Rauch, C.; Gehlhoff, W.; Wagner, M. R.; Malguth, E.; Callsen, G.; Kirste, R.; Salameh, B.; Hoffmann, A.; Polarz, S.; Aksu, Y.; Driess, M. Lithium Related Deep and Shallow Acceptors in Li-Doped ZnO Nanocrystals. *J. Appl. Phys.* **2010**, *107*, 024311.
(49) Çelik, Ö.; Baturay, Ş.; Ocak, Y. S. Sb Doping Influence on Structural Properties of ZnO Thin Films. *Mater. Res. Express* **2020**, *7*, 026403.
(50) Mendoza-Galván, A.; Trejo-Cruz, C.; Lee, J.; Bhattacharyya, D.; Metson, J.; Evans, P. J.; Pal, U. Effect of Metal-Ion Doping on the Optical Properties of Nanocrystalline ZnO Thin Films. *J. Appl. Phys.* **2006**, *99*, 014306.
(51) Glasscock, J. A.; Barnes, P. R. F.; Plumb, I. C.; Savvides, N. Enhancement of Photoelectrochemical Hydrogen Production from Hematite Thin Films by the Introduction of Ti and Si. *J. Phys. Chem. C* **2007**, *111*, 16477−16488.
(52) Bersani, D.; Lottici, P. P.; Montenero, A. Micro-Raman investigation of iron oxide films and powders produced by sol-gel syntheses. *J. Raman Spectrosc.* **1999**, *30*, 355−360.
(53) Fu, Y. Y.; Wang, R. M.; Xu, J.; Chen, J.; Yan, Y.; Narlikar, A. V.; Zhang, H. Synthesis of large arrays of aligned α-Fe2O3 nanowires. *Chem. Phys. Lett.* **2003**, *379*, 373−379.
(54) Jubb, A. M.; Allen, H. C. Vibrational Spectroscopic Characterization of Hematite, Maghemite, and Magnetite Thin Films Produced by Vapor Deposition. *ACS Appl. Mater. Interfaces* **2010**, *2*, 2804−2812.
(55) Joseph, J. A.; Nair, S. B.; Mary, S. A.; John, S. S.; Shaji, S.; Philip, R. R. Influence of Magnesium Doping on the Photocatalytic and Antibacterial Properties of Hematite Nanostructures. *Phys. Status Solidi B* **2022**, *259*, 2100437.
(56) Xiao, C.; Zhou, Z.; Li, L.; Wu, S.; Li, X. Tin and Oxygen-Vacancy Co-Doping into Hematite Photoanode for Improved Photoelectrochemical Performances. *Nanoscale Res. Lett.* **2020**, *15*, 54.
(57) Zhu, C.; Li, C.; Zheng, M.; Delaunay, J.-J. Plasma-Induced Oxygen Vacancies in Ultrathin Hematite Nanoflakes Promoting Photoelectrochemical Water Oxidation. *ACS Appl. Mater. Interfaces* **2015**, *7*, 22355−22363.
(58) Sima, M.; Matei, E.; Vasile, E.; Preda, N.; Logofatu, C. Water Oxidation at Photoanodes Based on Hematite Films and Nanowire Arrays. *Thin Solid Films* **2021**, *724*, 138626.
(59) Wang, R. X.; Beling, C. D.; Fung, S.; Djurišić, A. B.; Ling, C. C.; Kwong, C.; Li, S. Influence of Annealing Temperature and Environment on the Properties of Indium Tin Oxide Thin Films. *J. Phys. D: Appl. Phys.* **2005**, *38*, 2000−2005.
(60) Nogueira, A.; Santos Soares, M. R. S.; Souza Junior, J. B. S.; Ospina Ramirez, C. A. O.; Souza, F.; Leite, E. Discovering a Selective Semimetal Element to Increase Hematite Photoanode Charge Separation Efficiency. *J. Mater. Chem. A* **2019**, *7*, 16992−16998.
(61) Yi, J. B.; Lim, C. C.; Xing, G. Z.; Fan, H. M.; Van, L. H.; Huang, S. L.; Yang, K. S.; Huang, X. L.; Qin, X. B.; Wang, B. Y.; Wu, T.; Wang, L.; Zhang, H. T.; Gao, X. Y.; Liu, T.; Wee, A. T. S.; Feng, Y. P.; Ding, J. Ferromagnetism in Dilute Magnetic Semiconductors through Defect Engineering: Li-Doped ZnO. *Phys. Rev. Lett.* **2010**, *104*, 137201.
(62) Ullah Awan, S.; Hasanain, S. K.; Bertino, M. F.; Hassnain Jaffari, G. Ferromagnetism in Li Doped ZnO Nanoparticles: The Role of Interstitial Li. *J. Appl. Phys.* **2012**, *112*, 103924.
(63) Li, X.; Wang, Y.; Liu, W.; Jiang, G.; Zhu, C. Study of oxygen vacancies′ influence on the lattice parameter in ZnO thin film. *Mater. Lett.* **2012**, *85*, 25−28.
(64) Hardee, K. L.; Bard, A. J. Semiconductor Electrodes: V . The Application of Chemically Vapor Deposited Iron Oxide Films to Photosensitized Electrolysis. *J. Electrochem. Soc.* **1976**, *123*, 1024−1026.
(65) Dalle Carbonare, N. D.; Carli, S.; Argazzi, R.; Orlandi, M.; Bazzanella, N.; Miotello, A.; Caramori, S.; Bignozzi, C. A. Improvement of the Electron Collection Efficiency in Porous Hematite Using a Thin Iron Oxide Underlayer: Towards Efficient All-Iron Based Photoelectrodes. *Phys. Chem. Chem. Phys.* **2015**, *17*, 29661−29670.
(66) Dotan, H.; Sivula, K.; Grätzel, M.; Rothschild, A.; Warren, C. Probing the photoelectrochemical properties of hematite (α-Fe2O3) electrodes using hydrogen peroxide as a hole scavenger. *Energy Environ. Sci.* **2011**, *4*, 958−964.
(67) Iwanski, P.; Curran, J. S.; Gissler, W.; Memming, R. The Photoelectrochemical Behavior of Ferric Oxide in the Presence of Redox Reagents. *J. Electrochem. Soc.* **1981**, *128*, 2128.
(68) Dunn, K.; Feckl, M.; Müller, A.; Fattakhova-Rohlfing, D.; Morehead, G.; Roos, J.; Peter, M.; Scheu, C.; Bein, T. Tin Doping Speeds up Hole Transfer during Light-Driven Water Oxidation at Hematite Photoanodes. *Phys. Chem. Chem. Phys.* **2014**, *16*, 24610−24620.

https://doi.org/10.1021/acsomega.2c05241
ACS Omega 2023, 8, 2027−2033